Transport and Communications Science Journal

EFFECT OF GROOVE DEPTH ON DRAG AND AERODYNAMIC CHARACTERISTICS OF AXISYMMETRIC BOATTAIL MODELS WITH LONGITUDINAL GROOVES

Dam Vu Son Quyen[1], Nguyen Dinh Quang[2], Tran The Hung[2*]

[1]Hanoi Institute of Technology, Hanoi, Vietnam, No 3 Cau Vong, Duc Thang, Bac Tu Liem, Hanoi, Vietnam
[2]Le Quy Don Technical University, No 236 Hoang Quoc Viet Street, Bac Tu Liem, Hanoi, Vietnam

ARTICLE INFO

TYPE: Research Article
Received: 13/10/2024
Revised: 12/08/2025
Accepted: 11/09/2025
Published online: 15/09/2025
https://doi.org/10.47869/tcsj.76.7.2
[*] *Corresponding author*
Email: tranthehung_k24@lqdtu.edu.vn

Abstract. Reducing drag on boattail configurations remains a critical challenge in external aerodynamics. In this work, numerical simulations were conducted to examine the influence of longitudinal groove depth – represented by the groove-peak distance parameter A – on the flow behavior and drag characteristics of axisymmetric boattail bodies. The parameter A was varied between 0 and 0.3 times the body diameter (D). The computations employed the Reynolds-Averaged Navier–Stokes (RANS) equation for the similation. The k-ω SST turbulence model at a freestream velocity of 22 m/s. Results indicate that groove depth has negligible effect on drag at a 14° boattail angle, but at 18° a substantial reduction in drag of up to 11% was obtained for $A = 0.3D$. Analysis of pressure distribution, skin friction, and wake structure confirms that deeper grooves help suppress flow separation on the boattail surface. These findings highlight the importance of groove depth selection for optimizing aerodynamic efficiency in axisymmetric vehicles.

Keywords: RANS k-ω SST, longitudinal groove, axisymmetric boattail, flow separation.

1. INTRODUCTION

Aerodynamic drag associated with boattail afterbodies is a persistent issue in the design of axisymmetric flying vehicles. Flow separation at the aft region generates a broad wake and significant pressure deficit, which can contribute a large fraction of the overall drag. The near-wake behind boattails is recognized as one of the most complex flow regions in fluid dynamics [1]. Previous studies have reported that base drag may approach 50–60% of the total resistance for bodies with blunt or tapered tails [2,3]. This unfavorable flow also causes higher fuel consumption, structural vibration, and reduced stability, underscoring the need for effective drag-reduction strategies.

In unsteady states, flow separation at the tail not only increases drag but also leads to problems like higher fuel consumption, noise, vibration, structural damage, and instability [4]. For instance, the drag on a truck traveling at 100 km/h can consume up to 60% of its fuel [5]. The blunt shapes of buildings can induce significant oscillations when exposed to wind, affecting their efficiency, structural durability, and stability [4]. Thus, reducing drag and enhancing the performance of moving objects is critical in fluid mechanics and has garnered significant interest from scientists worldwide. Studies show that 10% reduction in drag can help 3.57% increase to 3.57% velocity [6]. Additionally, a 40% reduction in drag can save up to 50% in energy consumption.

To reduce drag, a moving object must be designed with a streamlined shape. In their study [7], Tran et al. demonstrated that incorporating a boattail is an effective method for reducing drag in blunt models. By examining boattail angles ranging from 0º to 24º, they found that drag was minimized at an angle of 14º. However, significant flow separation persisted, particularly at larger angles between 18º and 24º, limiting further reductions in total drag. As a result, further research is necessary to explore solutions for minimizing flow separation and drag in boattail designs.

Introducing grooves along the boattail surface has been recognized as a practical approach for drag mitigation. Howard et al. [8] first suggested applying such grooves to axisymmetric bodies and, through smoke-visualization experiments, showed that longitudinal grooves can suppress flow separation and consequently lower drag. More recently, Mariotti et al. [9,10] investigated transverse grooves on symmetric bodies and reported that they help delay flow detachment at the tail, thereby improving pressure recovery. Nevertheless, these studies were limited to certain boattail angles and did not provide a comprehensive assessment of groove parameters or guidelines for their optimal design.

Quang et al. [11] also developed a research model to study the impact of longitudinal grooves on drag and wake flow behind axisymmetric boattail bodies. Their results indicated that using longitudinal grooves smooths the flow, reduces flow separation, and increases surface pressure distribution on the tail. Consequently, aerodynamic drag was reduced by approximately 6% for a boattail angle of 14° and up to 24% for a boattail angle of 22°. However, the characteristics of groove parameters were not fully explored.

Recognizing the potential of using longitudinal grooves to reduce drag in boattail models, this study extends previous research by conducting a detailed analysis of how groove depth affects drag and aerodynamic flow characteristics around the boattail of axisymmetric models. This will provide a clear more comprehensive understanding of the effects of longitudinal grooves and offer recommendations for their application.

2. NUMERICAL METHOD

2.1. Model geometry

The axisymmetric boattail configuration and computational domain employed in this study is presented in Figure 1. The model has a body diameter D = 30 mm and an overall length L = 251 mm. The forebody adopts an elliptical nose to reduce potential flow separation, while the afterbody consists of a conical boattail with length $L_b = 0.7D$ and angle β = 14º and 18º. These geometric choices are consistent with earlier investigations [7,12,13], ensuring comparability of the numerical results. A uniform inlet velocity of $U_\infty = 22$ m/s was prescribed at a location $17D$ upstream of the model nose. Based on the body diameter, the corresponding Reynolds number is Re = 4.34×10^4. Symmetry conditions were imposed on the lateral boundaries of the domain.

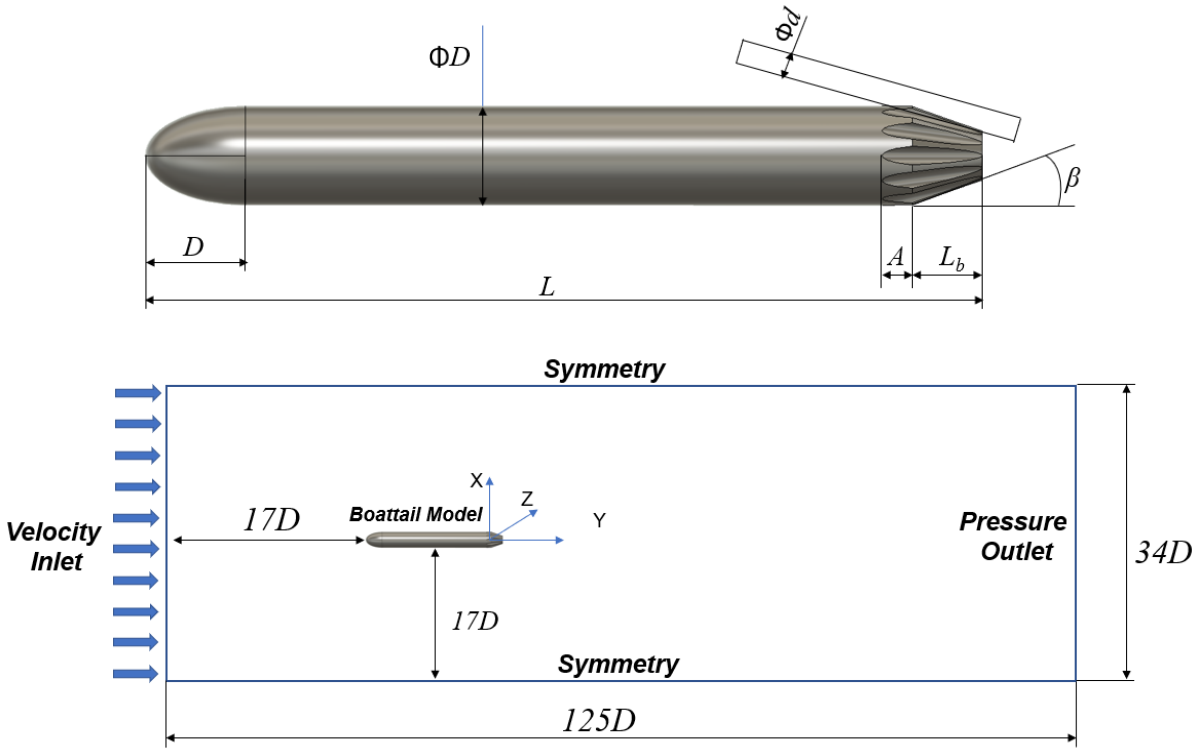

Figure 1. Geometry and computational domain.

Table 1. Research models paramters

Diameter of the model (D)	30 mm
Length of the model (L)	251 mm
Boattail length (L_b)	21 mm
Boattail angles (β)	14º, 18º
Diameter of grooves (d)	6 mm
Groove-peak distance (A)	0 ÷ 9 mm
Number of grooves (n)	12

Longitudinal grooves were introduced on the boattail surface. Each groove is defined by its diameter *d*, the distance from the groove peak to the surface denoted as parameter *A*, and the total number of grooves *n*. In this work, *A* is treated as the depth of the groove: larger values of *A* correspond to deeper penetration into the boattail surface. The grooves intersect the junction between the boattail and the base. To isolate the influence of depth, the groove diameter and number were fixed at $d = 6$ mm and $n = 12$. The parameter *A* was varied from 0 to 9 mm (equivalent to 0–0.3*D*). This range was selected to maintain the external shape of the baseline model while allowing a meaningful assessment of depth effects. The full set of model parameters is listed in Table 1.

2.2. Numerical scheme and meshing

The aerodynamic flow fields were obtained using the Reynolds-Averaged Navier–Stokes (RANS) approach with the k–ω SST turbulence model [14]. The governing equations can be represented as follows:

$$\frac{\partial \rho}{\partial t} + \frac{\partial}{\partial x_i}\left(\rho u_i\right) = 0 \tag{1}$$

$$\frac{\partial}{\partial t}\left(\rho u_i\right) + \frac{\partial}{\partial x_j}\left(\rho u_i u_j\right) = -\frac{\partial p}{\partial x_i} + \mu \frac{\partial}{\partial x_j}\left(\frac{\partial u_i}{\partial x_j} + \frac{\partial u_j}{\partial x_i}\right) + \frac{\partial}{\partial x_j}\left(-\rho \overline{u_i' u_j'}\right) \tag{2}$$

Here: $i, j = 1, 2, 3$; u_i is the average velocity component in each direction, p is pressure, ρ is air density; μ is the dynamic viscosity of air, taken as $\mu = 1.789 \times 10^{-5}$ kg/(m.s) at 25°C for the present simulations; $-\rho \overline{u_i' u_j'}$ is Reynolds Shear Stress.

Additional equations of parameter *k* and ω are shown as:

$$\frac{\partial\left(\rho k\right)}{\partial t} + \frac{\partial\left(\rho u_j k\right)}{\partial x_j} = P + \beta^* \rho \omega k + \frac{\partial}{\partial x_j}\left[\left(\mu + \sigma_k \mu_t\right)\frac{\partial k}{\partial x_j}\right] \tag{3}$$

$$\frac{\partial\left(\rho \omega\right)}{\partial t} + \frac{\partial\left(\rho u_j \omega\right)}{\partial x_j} = \frac{\gamma}{\nu_t} P - \beta \rho \omega^2 + \frac{\partial}{\partial x_j}\left[\left(\mu + \sigma_k \mu_t\right)\frac{\partial \omega}{\partial x_j}\right] + 2\left(1 - F_1\right)\frac{\rho \sigma_{\omega 2}}{\omega}\frac{\partial k}{\partial x_j}\frac{\partial \omega}{\partial x_j} \tag{4}$$

Here, ν_t is the turbulent viscosity due to eddy viscosity, represented as follows:

$$\nu_t = \frac{a_1 k}{\max(a_1 \omega; \Omega F_2)} \tag{5}$$

Where, *P* denotes the production term of turbulent kinetic energy, while $\sigma_k, \sigma_{\omega 2}, \beta, \beta^*, k, \gamma$ are model constants, specified with different values for near-wall and free-stream regions.

The simulations were conducted using licensed Ansys Fluent software at Le Quy Don Technical University. The COUPLED algorithm was selected to enhance the accuracy of the calculations. The simulation residuals reached a convergence level of 10^{-6}, thereby increasing the reliability of the simulation results.

An unstructured mesh was generated for the computational domain. The surface mesh of the model is illustrated in Figures 2(a, b). To ensure adequate resolution for the *k–ω* SST turbulence model, the first cell height adjacent to the wall was set to 8.5×10^{-5} m, with a growth rate of 1.18 applied to the subsequent layers. This arrangement produced wall-normal resolutions corresponding to y^+ values on the body surface below 6 in Figure 2(c), which is appropriate for the selected turbulence model.

The computational volume is discretized using an unstructured mesh. The mesh on the surface of the model is depicted in Figure 2(a) and 2(b). To accommodate the *k-ω* SST turbulence model, the thickness of the first mesh layer from the model surface is set to 8.5×10^{-5} m, with a growth rate of 1.18 for subsequent layers. This configuration results in the y+ values on the surface of the model, as shown in Figure 2(c), with the maximum value being approximately 6, suitable for the selected turbulence model.

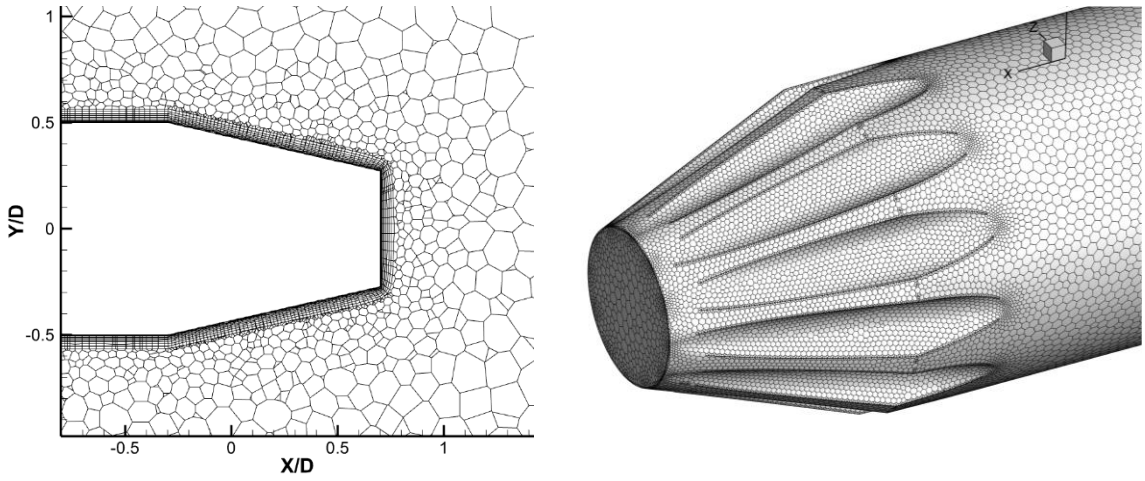

(a) Mesh around boattail (b) Surface mesh

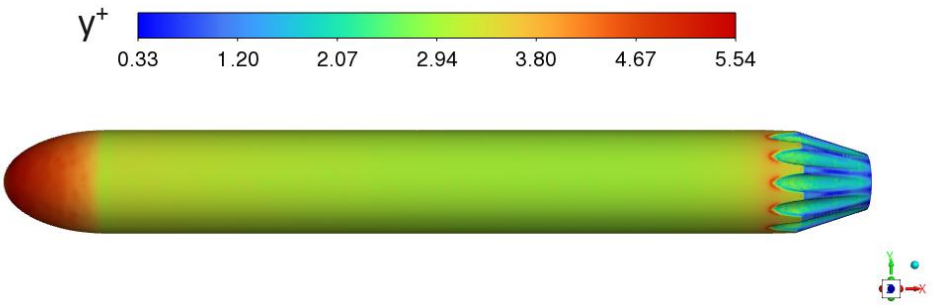

(c) y^+ value

Figure 2. Mesh structure and y^+ values.

To verify mesh convergence, the research team conducted a grid independence check by progressively increasing the number of mesh elements from 0.64 million to 4.95 million. This check was performed for the boattail model with β = 20° and without grooves (A = 0 mm). This configuration was chosen because experimental results for the same 20° boattail model

are available from Tran et al. [7], enabling direct comparison and validation of the numerical approach. The mesh independence study confirmed that beyond 3.70 million elements, the solution remained essentially unchanged (Table 2). Consequently, the grid with 3.70 million cells was adopted for subsequent simulations, providing a balance between accuracy and computational efficiency.

Table 2. The influence of mesh cells on drag force.

Number of cells	0.64	1.4	2.0	2.7	3.7	4.95
Drag coefficient (C_D)	0.25893	0.25576	0.25399	0.25286	0.2519	0.25171

The validation in this study was performed by comparing with experimental data from Tran et al. [7], obtained using a magnetic suspension and balance system (MSBS) in a low-speed wind tunnel at Tohoku University, Japan. This facility enables free-levitated drag measurements without support interference, providing high-accuracy aerodynamic data. The validation model used was a boattail without grooves (baseline model). The validation results are shown in Table 3. It can be observed that the error of the computational model in this study is very close to the published results of Tran et al., with errors for the 14º and 18º boattail angles being only 1.7% and 1.3%, respectively. This confirms the reliability of the computational model used in this study, making it fully applicable for calculations involving grooved models.

Table 3. Validation of drag coefficient against the findings by Tran [14].

Boattail angle (β)	14º	18º
Tran et al. [13]	0.22633	0.24438
Current work	0.22247	0.24123
Error (%)	1.7	1.3

3. RESULTS AND DISCUSSION

3.1. Influence of groove-peak distance A on drag coefficient

The graph showing a influence of the drag on the distance A for the axisymmetric boattail models is presented in Figure 3. Here, the model without grooves corresponds to $A = 0D$, while the grooved model has A values ranging from $0.1D$ to $0.3D$. It can be observed that, while the drag coefficient does not change significantly for the 14° boattail angle, it decreases considerably for the 18° boattail angle as A increases. The drag reduction reaches up to 11% when $A = 0.3D$. This is quite interesting and may be due to the fact that longitudinal grooves have a more significant effect at larger boattail angles. These findings align closely with those of Quang et al. [11], where longitudinal grooves were found to be most effective at larger boattail angles, offering minimal benefit at smaller angles, particularly below 14º. However, this study reveals that the extent of drag reduction depends on variations in the groove depth parameter. As A increases, drag decreases, but the rate of reduction diminishes progressively, as shown in Table 4. From these results, designers can select appropriate groove parameters,

such as choosing A = 3 mm to achieve a 7% drag reduction, rather than tripling A to 9 mm for only an additional 4% reduction. Similarly, for smaller boattail angles, increasing A provides negligible improvement in drag reduction.

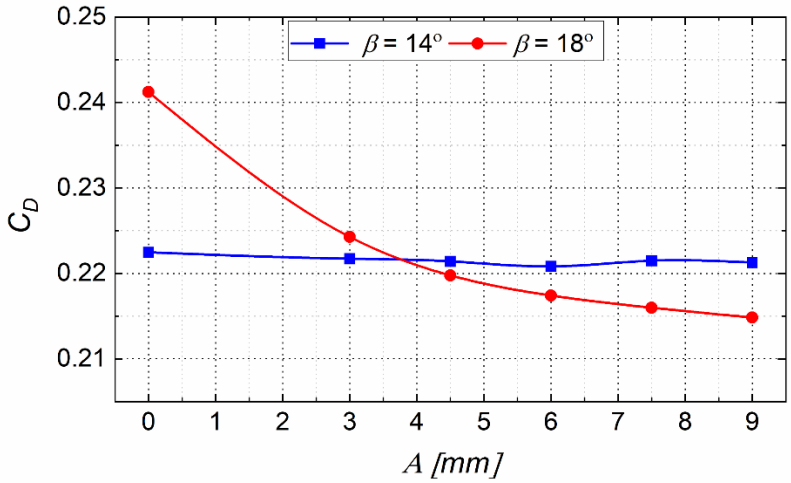

Figure 3. Influence of parameter A on drag coefficient.

Table 4. Drag reduction by A for 18-degree boattail model.

***A* (mm)**	3	4,5	6	7.5	9
Reduction (%)	7.0	8.9	9.9	10.5	10.9

Figure 4 shows how the drag components vary with changes in A. As A increases, the skin-friction drag component grows slightly, while the pressure drag component reduces significantly, driving the overall reduction in total drag for the model.

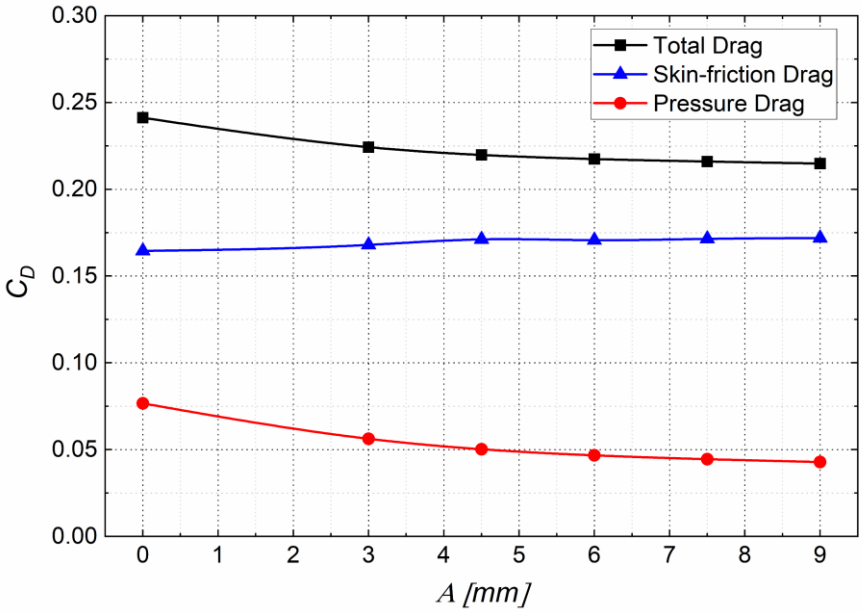

Figure 4. Drag components of 18-degree boattail model.

3.2. Distribution of skin-friction coefficient along the boattail surface

Figure 5 shows the streamwise skin friction C_f in the grooved region for models with grooves at different distances A from the groove peak and compares it with the baseline model without grooves at the same location. It is observed that, for the grooved cases, the C_f tends to peak at the groove peak and then decrease over the boattail region but still maintains positive values. This indicates that no flow separation is generated on the boattail surface in the presence of grooves. However, differences arise in the baseline case. For the model of 14°, flow separation only occurs in a small area near the boattail peak, while for the 18° boattail angle, complete flow separation occurs over the entire boattail. This explains why drag changes significantly with the presence of grooves at the 18° boattail angle.

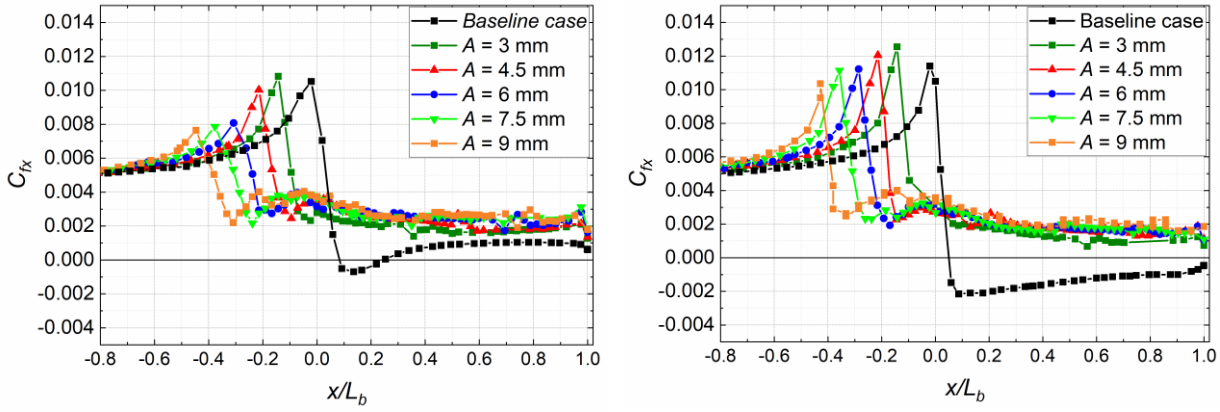

(a) 14º (b) 18º

Figure 5. Distribution of skin-friction coefficient along the boattail surface.

3.3. Flow structures in the boattail region

To further investigate the impact of grooves with different groove-peak distances A on drag, we analyzed the flow over the boattail surface and afterbody, as presented in Figure 6. It can be seen that at a 14° boattail angle, there is no significant difference in flow structure as A changes. However, for the 18° case, the flow becomes smoother and the size of the wake vortex behind the boattail significantly reduces when grooves are present compared to the baseline case. This again confirms the effectiveness of longitudinal grooves at larger boattail angles.

In Figure 7, the velocity profile along the centerline is presented. It is observed that as the value of A increases, the change in the velocity profile remains minimal. The location of the recirculation point, in which the relative velocity shifts from negative to positive, is nearly identical across all grooved cases. However, for the 18° boattail angle, the distance between the recirculation points of the grooved and ungrooved cases is larger compared to the 14° boattail angle.

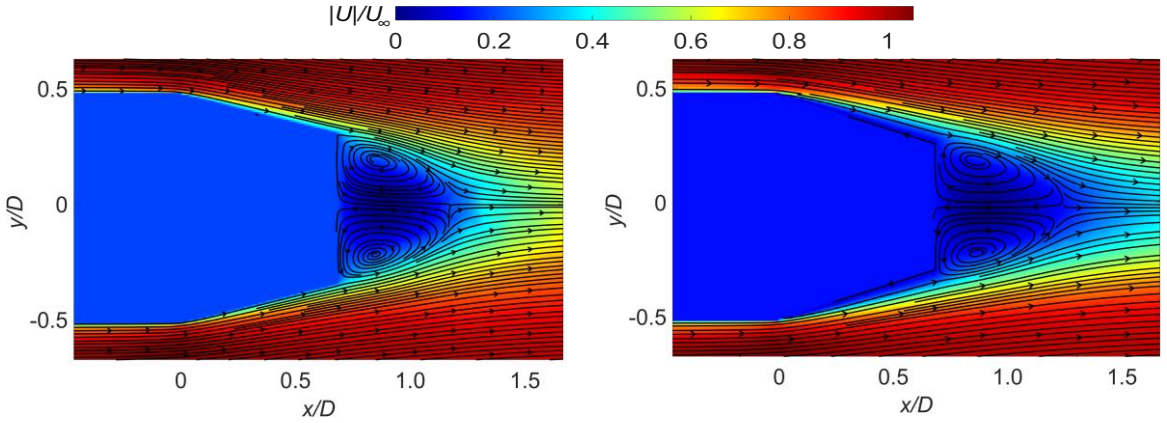

(a) Baseline case

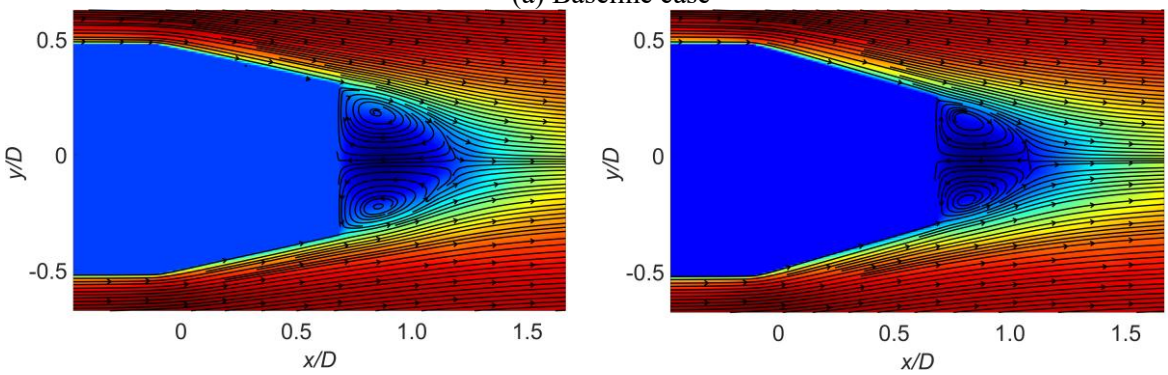

(b) A = 3 mm

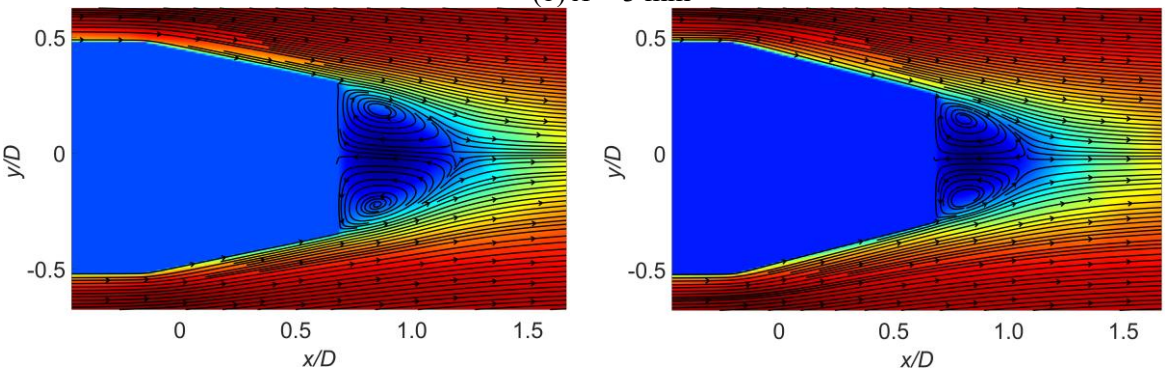

(c) A = 6 mm

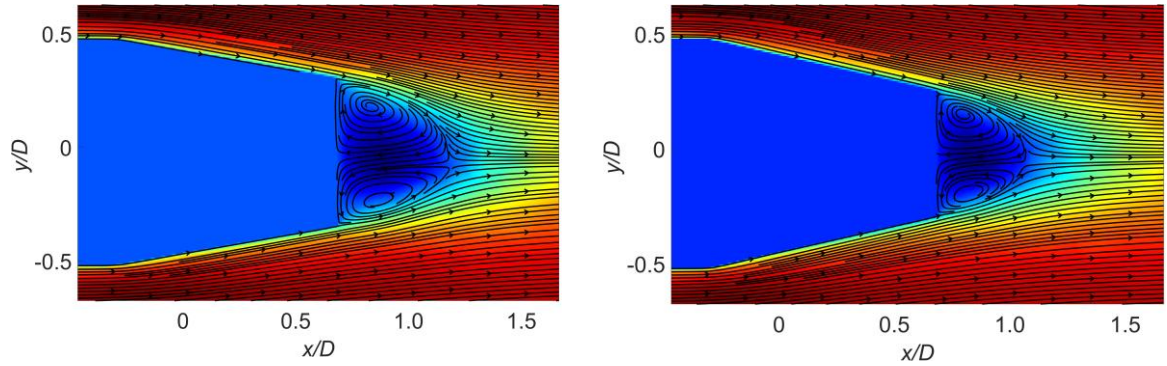

(c) *A = 9 mm*

Figure 6. Flow structure around boattail for 14-degree models (left) and 18-degree models (right).

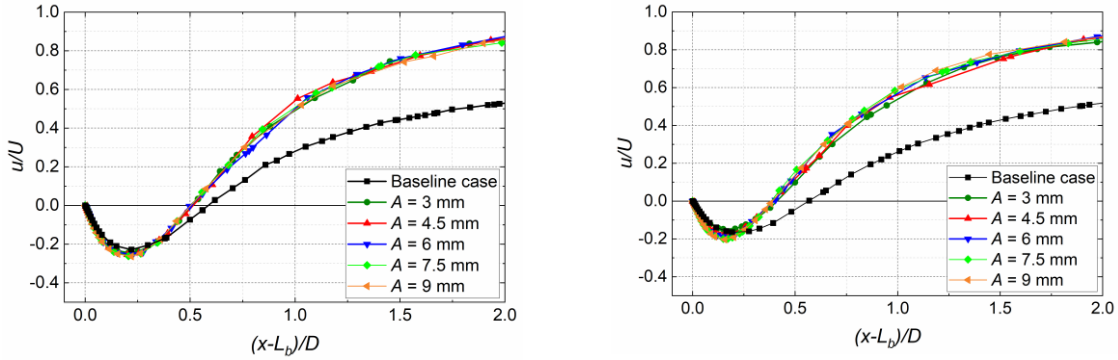

(a) 14º (b) 18º

Figure 7. Velocity at centerline for different parameter A.

3.4. Pressure distribution on the boattail region

The pressure coefficient C_p of the models with boattail angles of 14° and 18° is plotted in Figure 8 at the plane passing through the groove, as the groove-peak distance A varies. It can be observed that the pressure coefficient C_p reaches its lowest value near the boattail peak before rising again. As A changes, the corresponding bottom region shifts forward, which is understandable due to the geometric alterations of the body when A increases. However, it is also noted that the minimum C_p tends to increase as A increases. This is because increasing A reduces the boattail angle at the groove region, leading to smoother flow over the boattail peak, thereby increasing C_p in that area and narrowing the low-pressure region.

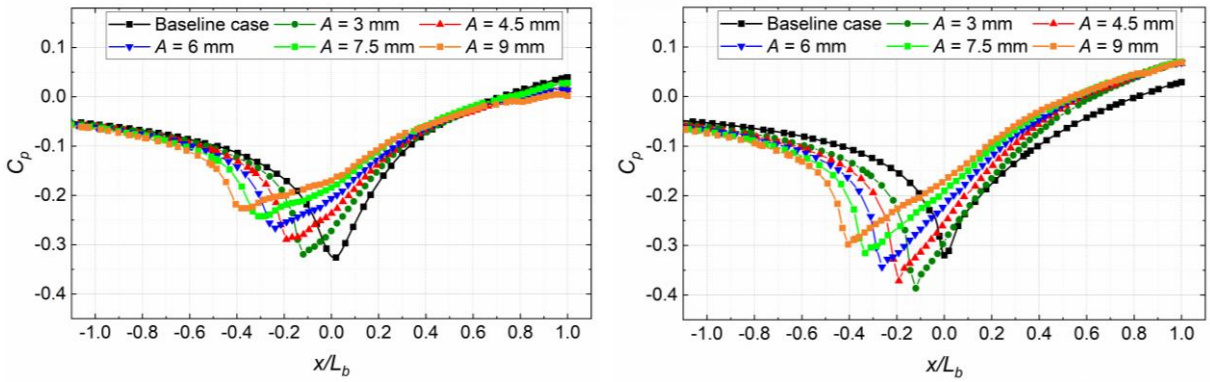

(a) 14º (b) 18º

Figure 8. Pressure distribution along boattail region.

Additionally, it is observed that although the pressure at the boattail peak region in the models with an 18° boattail angle is lower than in the 14° case, the pressure on the boattail surface rises more quickly and reaches a higher value at the base. This growth in base pressure is the main reason for the decreasing drag in the 18° boattail case.

4. CONCLUSION

This work has examined how the depth of longitudinal grooves, expressed by the groove-peak distance parameter A, influences the aerodynamic performance of axisymmetric boattail bodies. Simulations were performed for boattail angles of 14º and 18º with A varying up to 0.3D. The analysis of pressure distribution, velocity field, and wall shear stress provided physical insight into the resulting drag trends.

The results show that for the smaller boattail angle of 14º, changes in groove depth have little effect on overall drag. In contrast, at 18º, increasing A substantially alleviates separation and reduces drag, reaching a maximum reduction of about 11% at A = 0.3D. This confirms that groove depth is a critical parameter governing the effectiveness of drag reduction for steeper boattails.

From a design perspective, longitudinal grooves offer a practical means of improving aerodynamic efficiency without altering the external shape significantly. The present findings highlight the role of groove depth in tailoring such modifications. Nonetheless, other geometric factors – including groove diameter, number of grooves, and boattail angle – also merit further investigation to identify optimal configurations. In addition, because the present work relied on steady RANS simulations, future studies employing URANS or LES are recommended to capture unsteady wake structures and validate the robustness of these conclusions.

ACKNOWLEDGMENT

Nguyen Dinh Quang was funded by the Master, PhD Scholarship Program of Vingroup Innovation Foundation (VINIF), code VINIF.2024.TS.086.

REFERENCES

[1]. R. Merz, R. Page, and C. Przirembel, Subsonic axisymmetric near-wake studies, AIAA journal, 16 (1978) 656–662.
[2]. R. J. Krieger, S. R. Vukelich, Tactical missile drag, tactical missile aerodynamics, Progress in Astronautical Aeronautic AIAA, 104 (1986) 383–420.
[3]. P. R. Viswanath, Flow management techniques for base and afterbody drag reduction, Progress in Aerospace Science, 32 (1996) 79–129. http://doi.org/10.1016/0376-0421(95)00003-8
[4]. G. Rigas, A. Oxlade, A. Morgans, and J. Morrison, Low-dimensional dynamics of a turbulent axisymmetric wake, Journal of Fluid Mechanics, 755 (2014) R5.
[5]. W. Jiajan, R. Chue, T. Nguyen, and S. Yu, Boattail juncture shaping for spin-stabilized rounds in supersonic flight, Shock Waves, 25 (2015) 189–204.
[6]. L. Wu, Experimental investigations on drag-reduction characteristics of bionic surface with water-trapping microstructures of fish scales, Scientific Reports, 8 (2018) 12186.
[7]. T.H. Tran, H.Q. Dinh, H.Q. Chu, V.Q. Duong, C. Pham, V.M. Do, Effect of boattail angle on near-wake flow and drag of axisymmetric models: a numerical approach, Journal of Mechanical Science and Technology, 35 (2021) 563–573. http://doi.org/10.1007/s12206-021-0115-1
[8]. F. G. Howard, W. L. Goodman, Axisymmetric bluff-body drag reduction through geometrical modification, Journal of Aircraft, 22 (1985) 516–522. http://doi.org/10.2514/3.45158
[9]. A. Mariotti, G. Buresti, G. Gaggini, M.V. Salvetti, Separation control and drag reduction for boat-tailed axisymmetric bodies through contoured transverse grooves, Journal of Fluid Mechanics, 832 (2017) 514–549. http://doi.org/10.1017/jfm.2017.676
[10]. A. Mariotti, G. Buresti, M.V. Salvetti, Separation delay through contoured transverse grooves on a 2D boat-tailed bluff body: Effects on drag reduction and wake flow features, European Journal of

Mechanics-B/Fluids, 74 (2019) 351–362. https://doi.org/10.1016/j.euromechflu.2018.09.009
[11]. N.D. Quang, T.H. Tran, D.A. Le, N.T Hieu, V.K Pham, T.S Ha, Drag reduction for axisymmetric boattail model by longitudinal groove cavity under low-speed conditions, Journal of Mechanical Science and Technology, 38 (2024) 4209–4220. https://doi.org/10.1007/s12206-024-0718-4
[12]. T.H. Tran, T. Ambo, T. Lee, L. Chen, T. Nonomura, K. Asai, Effect of boattail angles on the flow pattern on an axisymmetric afterbody surface at low speed, Experimental Thermal and Fluid Science, 99 (2018) 324–335. http://doi.org/10.1016/j.expthermflusci.2018.07.034
[13]. T.H. Tran, T. Ambo, T. Lee, T. Ozawa, L. Chen, T. Nonomura, K. Asai, Effect of Reynolds number on flow behavior and pressure drag of axisymmetric conical boattails at low speeds, Expriments in Fluids, 60 (2019) 1–19. http://doi.org/10.1007/s00348-019-2680-y